DEMONSTRATION OF AN AUTOMATED CFD SYSTEM FOR THREE-DIMENSIONAL FLOW SIMULATIONS[1]

J.W. van der Burg, J.E.J. Maseland, R. Hagmeijer, K.M.J. de Cock,
National Aerospace Laboratory NLR,
Anthony Fokkerweg 2,
1059 CM Amsterdam, The Netherlands.

ABSTRACT

In this paper the capabilities of an automated CFD system which is currently available at NLR are demonstrated. Transonic flow around the AS28G wing/body configuration and hypersonic flow through a generic three-dimensional mixed-compression airbreathing inlet are simulated. An assessment of the level of automation of the current CFD-system is made. The problem-turnaround time lies within the order of a week for both applications.

1. INTRODUCTION

Experience with CFD technology (multiblock structured grid methods) learns that the turnaround time for generation of grids for Euler/Navier-Stokes calculations of complex aircraft configurations is large. In order to efficiently contribute to aircraft design the problem-turnaround time must be reduced to the order of a day or a week [1]. Unstructured grid methods offer the possibility to bring about this reduction.
The level of acceptance of CFD technology in the aerodynamic design process is directly related to the ability to produce accurate solutions. High accuracy of aerodynamic forces is especially important so that the computed lift, drag and pitching moment can be relied upon to reduce the risks involved in aircraft design.
In view of these aspects DLR and NLR started a cooperation entitled "CFD for complete aircraft" to develop a fully automatic system for three-dimensional flow simulations. The algorithms used are based on the unstructured grid approach [2] which is based on a Galerkin finite-element method to discretise the three-dimensional Euler equations.

The objective of this paper is to demonstrate the capabilities of the CFD system which is currently available at NLR. The focus will be on the level of automation and accuracy of the CFD system. The first application concerns three-dimensional transonic inviscid flow past the AS28G-wing/body configuration. The second application is the study of an airbreathing inlet, which is part of the AEOLUS programme, a joint industry project in the Netherlands [3]. The CFD system is used to simulate hypersonic inviscid flow (no real gas effects included) through a generic three-dimensional mixed-compression inlet with two ramps.

2. CFD SYSTEM AT NLR

At NLR an automated CFD-system for three-dimensional inviscid flow simulations is acquired. In the current CFD-system the following algorithmic steps are necessary to obtain a visual representation of the flow field for a given aircraft configuration.

   1. Geometry definition.

---

2. Surface triangulation.

3. Three-dimensional grid generation.

4. Pre-processing.

5. Flow calculation.

6. Grid adaption.

7. Visualisation and post-processing.

The algorithmic steps 2-6 are fully automated, i.e. extensive user interaction is not required for these steps. In this section these algorithmic steps are discussed.

2.1 Geometry definition

The geometry of an aircraft configuration is usually defined using a CAD system (e.g. ICEM-CFD) and described in a standard data format. Typically, the geometry is established in terms of geometric entities, viz. support surfaces and curves. The relation between these geometric entities, referred to as the topology, has to be defined explicitly. The respective entities are then modelled by means of piecewise cubic surface and curve representations.

At present an application starts either with a user-defined aircraft configuration or an aircraft configuration abstracted from a three-dimensional multi-block grid [4]. By adding the geometry description of far field boundaries and the symmetry plane (optional) a three-dimensional flow domain enclosed by bounding surfaces is defined. In such a way the boundaries of the flow domain are fully defined.

2.2 Surface triangulation

In order to perform a flow calculation the flow domain has to be discretised, i.e. boundaries are triangulated and a tetrahedral grid is generated in the interior of the flow domain. Firstly, the boundaries of the flow domain are discretised resulting in a surface triangulation. To this purpose a *surface triangulation algorithm* is employed which incorporates an equi-distribution algorithm for discretising curves and an advancing front-type generation algorithm for discretising surfaces. A distribution function controls the size of the edges and triangles in the surface triangulation.

This distribution function is defined by parameters which are specified in the background grid and in source terms. Source terms are introduced in regions to refine regions of special interest. The distribution function expresses a desired spacing in each point of the flow domain.

2.3 Three-dimensional grid generation

Subsequently, a three-dimensional grid of Delaunay-type is obtained by employing a *three-dimensional grid generation algorithm*. In this algorithm a prospective node is located at the barycenter of a tetrahedron. If this prospective node satisfies the Delaunay criterion the node is inserted and connected to the existing tetrahedral grid. In case the grid size, due to insertion of this node, becomes to small the prospective node is rejected. Smoothness of the three-dimensional grid is treated explicitly by the distribution function (as defined by the background grid and source terms). As a result a three-dimensional tetrahedral grid is generated which is bounded by a topologically two-dimensional surface triangulation.

2.4 Pre-processing

The next algorithmic step is the *pre-processing algorithm*. This algorithm is designed to optimise the flow calculation for the generated three-dimensional grid. By employing a colouring algorithm for the edges in the three-dimensional grid a high degree of vectorisation in the flow calculation can be reached.

2.5 Flow calculation

In the *flow calculation algorithm* three-dimensional inviscid flow is simulated. The incorporation of an upwind solver makes the CFD-system suited for the simulation of subsonic, transonic, supersonic as well as hypersonic flows. For the spatial discretisation of the three-dimensional Euler equations Roe's approximate Riemann solver [5] is utilised. Second-order accuracy is achieved by employing a MUSCL interpolation [6] for the state vectors, following the approach in [7, 8]. An entropy fix is incorporated to prevent physically incorrect features in a numerical solution. At present the boundary conditions are treated with first-order accuracy. Time integration is established by adopting a Runge-Kutta time step algorithm. Convergence acceleration is achieved by local time stepping and residual averaging.

2.6 Grid adaption

In case the flow calculation has sufficiently converged (by taking a large number of Runge-Kutta time steps) the *grid adaption algorithm* can be employed. The grid adaption algorithm is based on remeshing. Based on the values of an adaption variable (for instance: density, Mach number or pressure coefficient) an adaption indicator is calculated which is based on the undivided difference of this adaption variable. According to the value of the adaption indicator sources terms are generated which are utilised to adapt the surface triangulation. Subsequently, the three-dimensional grid generation algorithm is adopted to generate an entire new three-dimensional grid. By incorporating the newly generated source terms in the existing distribution function a locally refined grid is obtained. For the adapted grid a numerical solution is then obtained by first employing the pre-processing algorithm and subsequently the flow calculation algorithm. This process can be repeated until a numerical solution of sufficient accuracy is obtained.

2.7 Visualisation and post-processing

Finally, a *post-processing algorithm* is adopted to calculate aerodynamic quantities. Flow visualisation is achieved by using the commercial package Data Visualiser [9]. Interfaces are available to visualise the geometry definition, the surface triangulation and the numerical solution.

3. APPLICATIONS

This section discusses two applications of the current CFD system at NLR. The first application concerns transonic flow around a wing/body configuration and the second application concerns hypersonic flow for a generic three-dimensional mixed-compression airbreathing inlet configuration.

3.1 AS28G wing/body configuration

In the first application described here inviscid flow around the AS28G wing-body configuration is simulated. The geometry is defined by 14 support surfaces and 42 curves. The physical coordinates of these support surfaces and curves are abstracted from a multi-block grid. The support surfaces contain approximately 17000 nodes. Far field boundaries and a symmetry plane are incorporated to define a closed flow domain.

The surface triangulation shown in figure 2 is obtained. It can be observed that the nose region,

tail region, wing leading edge, trailing edge and the tip are refined. Source terms are located in these regions in order to obtain sufficient resolution of the geometry of the AS28G wing/body configuration and to reduce expected losses in total pressure.

One successive refinement is employed. The surface triangulation of the adapted grid is shown in figure 3. The dimensions of the surface triangulation and the three-dimensional grid for the initial and the adapted grid can be found in table 1. The problem size for the adapted grid is approximately two times larger in comparison with the initial. Cpu-times for the respective algorithmic steps are shown in table 2 and the convergence history is depicted in figure 1.

In the flow calculation a three-step Runge-Kutta time step scheme with a CFL-number of 0.9 is utilised. Two jacobi iterations are employed to smooth the residuals. The flow calculation algorithm uses 81 words per grid node, which is relatively large [10], and reaches a performance of 253 Mflops on the NEC SX3.

The Mach-number and total pressure distribution are shown in figures 4 and 5 respectively. A relatively small amount of grid points is necessary to resolve the lambda shock on the upper side of the wing. This is a promising result as for instance in a multi-block structured code more grid points are necessary to capture the same shock structure. Nevertheless, large losses in total pressure ($\pm 25\%$) are experienced at the leading edge of the wing. This is mainly due to fact that the boundary condition at the wing is only first-order accurate. A relative large loss in total pressure is also observed on the upper side of the wing (8%).

3.2 Three-dimensional mixed compression airbreathing inlet

One of the most critical enabling technologies of advanced reusable launchers is the propulsion system. For example a two-stage-to-orbit aerospace vehicle needs a propulsion system to power the vehicle from take-off to sustained flight at Mach numbers ranging from 6 to 7 (separation Mach number of the rocket powered second stage from the airbreathing first stage). Sustained flight of airbreathing aerospace vehicles at these Mach numbers is not feasible with todays technologies.

The inlet considered here is of mixed compression type [11, 12]. Before entering the inlet, the oncoming air is decelerated to a hypersonic Mach number lower than the flight Mach number by oblique shock waves (see figure 6). Near the narrowest duct cross section, the throat, the flow passes a normal shock wave. Behind this shock the flow is subsonic. Further deceleration is required to a velocity acceptable for the combustion chamber. The subsonic deceleration requires a diverging duct called the diffuser.

The present section discusses typical results for flow through the mixed compression airbreathing inlet. The geometry of the inlet is described in full detail in reference [13]. The inlet geometry is based on a two-dimensional design that has been obtained by using engineering tools. The inlet considered here is designed for a freestream Mach number of $M_\infty = 4.5$. The forebody of the space plane is not modelled. Hence, a Mach number smaller than the flight Mach number is considered. Bleed slots are not taken into account since viscosity is neglected. Both the cowl lip and the side wall are modelled with finite dimensions.

The geometry of the inlet is defined by 46 curves and 18 support surfaces. The geometry contains 16 planes and 2 cubic polynomial representations, namely the cowl lip and the leading edge of the side wall. Figure 7 shows an inside view of the inlet from the upstream direction. The cowl lip and the side walls are clearly visible. At the top of the figure two ramps can be observed. The large bounding planes at the right-hand and left-hand side are boundaries of the flow domain on which symmetry conditions are imposed. In the inlet duct the right-hand bounding plane is also defined as a symmetry plane. At the left-hand side the wall of the inlet duct can be observed. An impression of the surface triangulation on the side-wall (left-hand side of figure 7) is shown in figure 8. Sufficient grid points are generated to obtain an accurate representation of the cowl lip.

716

For the freestream Mach-number $M_\infty = 4.5$ a typical "unstart" condition is obtained, see figure 9. This means that there is a strong bow shock in front of the duct inflow plane providing subsonic flow throughout the duct. In windtunnel experiments a "started" condition is obtained by opening the throat significantly so that the shock can pass. Once the shock has been swallowed, the diffuser throat area is decreased, while simultaneously the pressure ratio of the pressure of the outlet of the diffuser with respect to the freestream pressure is increased so that the shock is caused to move to the diffuser throat [14].

During numerical simulations, however, the variation of the geometry is not trivial to simulate. To solve this problem the calculation is started with a higher Mach number $M_\infty = 5.0$ so that effective throat area is increased. This results in a globally correct pattern of oblique shock waves. The "unstart" condition is not experienced as the effective throat area is too wide for that particular Mach number. Subsequently, the Mach number is gradually lowered to the required value $M_\infty = 4.5$.

Moreover, to obtain the final shock in the diffuser throat and accordingly subsonic outflow, the pressure at the diffuser outlet has to be imposed. The location of the final shock is a function of the value of the pressure, which can be found by employing normal shock relations and using the fact that the flow is isentropic behind the final shock (see reference [15]).

Figure 10 shows a side view of the "started" condition with a final shock behind the throat of the duct. It can be observed that the oblique shocks and the final shock are resolved quite accurately.

4. LEVEL OF AUTOMATION

A reduction in CFD-problem-turnaround time can be achieved by an increased level of automation. This section will focus on the automation level of the current CFD system for the applications discussed in section 3. Those algorithmic steps in the current CFD system described in section 2 which require user-interaction are identified. This identification is necessary in order to assess the potential for an increased level of automation.

A With respect to geometry definition (step 1) an aircraft configuration is usually defined in terms of standard CAD data format. Extensive user interaction is required to generate a multi-block grid (such as for the wing/body configuration) which is suited as input for the current CFD-system. Consequently the problem-turnaround-time is large for multi-block based geometries.

B The definition of far field boundaries (step 1) (such as for the wing/body configuration) requires user interaction. The topology of a three-dimensional far field cube, the dimensions of the cube and the relation with between cube and the aircraft configuration have to be established.

C The definition of the distribution function (steps 2 and 3), which controls the size and shape of triangles in the surface triangulation and tetrahedral elements in the three-dimensional grid, requires user interaction. Visualisation of the generated surface triangulation is necessary in order to inspect the influence of the distribution function. A surface triangulation is accepted if sufficient resolution of details of the aircraft configuration (like wing leading and trailing edge) is obtained. After modification of the distribution function it is necessary to regenerate the surface triangulation. It is observed that the definition of a suitable distribution function does not guarantee a successful three-dimensional grid generation algorithm. An intolerably large number of tetrahedral elements may be generated in case parameters defining the distribution function are chosen too small. For the current CFD-system an expert user is required to specify the distribution function.

717

D It is necessary to define boundary types (like symmetry plane, far field or solid wall) for each surface of the flow domain (step 4). This requires only a relative small amount of user interaction.

E This requirement also holds for the specification of flow calculation parameters (step 5), such as for instance: Mach-number, angle of attack, CFL-number, number of Runge-Kutta time steps and Restart-option.

F Inspection of the flow solution by visualisation (step 7) can have a negative influence on the problem-turnaround-time if the number of nodes in the three-dimensional grid is large. This effect can be attributed to the fact that the handling of a large data-file in a multi-user environment and the operations necessary for visualisation, such as zooming, pivoting and moving, are relatively slow.

G In the grid adaption algorithm (step 6) user interaction is required to assess the level of grid refinement. Initially, default values for the grid adaption parameters are taken. Visual inspection then learns whether the surface triangulation has been adapted sufficiently. If the generated surface triangulation is not acceptable (for instance the level of refinement is too high) the grid adaption algorithm has to be repeated with modified input-parameters. Moreover, the number of nodes generated in the three-dimensional grid (after adaption, remeshing) is very sensitive to the values of the parameters specified in the grid adaption algorithm. If the number of nodes generated becomes too large it is necessary to repeat the grid adaption algorithm and the three-dimensional grid generation algorithm.

In the near future the focus is on the respective parts requiring extensive user interaction, namely items A, C and G. It is foreseen that the remaining items B, D and F requiring more than minimal user interaction can be automated.

By constructing an interface with a standard CAD data format the generation of a multi-block grid as input for the CFD-system can be avoided (item A). The data structure in the current CFD system is capable of handling a standard CAD data format. This would already significantly reduce the amount of user interaction.

The influence of the distribution function (background grid and source terms) and the grid adaption parameters on the three-dimensional grid generation algorithm remains difficult to estimate (item C and G). Ideally, a functional relationship between these parameters and the number of nodes generated in the three-dimensional grid could contribute here. However, for complex geometries this relationship is difficult to assess.

5. CONCLUSIONS

The capabilities of the CFD system have been demonstrated for two applications. For the AS28G wing/body configuration and the three-dimensional mixed compression airbreathing inlet configuration the results so far indicate the potential for short turnaround times. An assessment of those parts in the CFD system which require user interaction shows that the automation level can be increased. The actual problem-turnaround time (geometry definition, surface triangulation, 3D grid generation, flow calculation, grid adaption, flow visualisation and post-processing) lies in the order of a few days for both applications.

Moreover, the results indicate that the current CFD-system produces accurate solutions. The upwind-based flow calculation algorithm yields a spatially second-order accurate solution. However, the boundary conditions are currently only first-order accurate.

718

References

[1] P.E. Rubbert, "CFD and the changing world of airplane design", In *ICAS Proceedings, 19th Congress of the International Council of the Aeronautical Sciences*, September, 1994.

[2] N.P. Weatherill, O. Hassan, D.L. Marcum, "Calculation of steady compressible flow fields with the finite element method", AIAA 93-0341, 1993.

[3] R. Sudmeijer, W.B. de Wolf, "Research, Design and Development plan for the inlet system of an airbreathing launcher", 1993.

[4] J.W. Boerstoel, "A system of CFD codes for industrial CFD analysis of flows around aircraft including propulsion systems modelling", NLR CR 93-519 L, 1993.

[5] P.L. Roe, "Approximate Riemann solvers, parameter vectors and difference schemes", Journal of Computational Physics, 43:357 372, 1981.

[6] B. van Leer, "Towards the ultimate conservative difference scheme. V. A second-order sequel to Godunov's method", Journal of Computational Physics, 32:101 136, 1979.

[7] J.W. van der Burg, "Numerical techniques for transonic flow calculations", PhD thesis, University of Twente, Enschede, The Netherlands, 1993.

[8] K.M.J. de Cock, "Multigrid convergence acceleration for the 2D Euler equations applied to high lift systems", NLR TP 93301, 1993.

[9] Wavefront Technologies, Inc., Data Visualizer User's Guide, Fourth Edition, May 1993.

[10] T.A. Kinard, B.W. Harris, "Evaluation of two unstructured CFD methods", AIAA 94-1877, 1994.

[11] R. Hagmeijer, "Required tools for aerothermodynamic analysis and design of space plane engine intakes", AE-NLR-TN-9303 (1), 1993.

[12] R. Hagmeijer, B. Oskam, J.W. van der Burg, J.E.J. Maseland, K.M.J. de Cock, "Aerothermodynamic models of hypersonic flow and their application to the inlet flow of an airbreathing launcher", 1994.

[13] R.H.J. Oerlemans, "Geometric description of a generic space plane intake for CFD calculations and preliminary structural design work", AE-NLR-TN-9403 (1) in progress, 1994.

[14] M.J. Zucrow, J.D. Hoffman, "Gas Dynamics", Volume 1, John Wiley and Sons, Inc., 1976.

[15] B.G. ten Wolde, "Flow calculations for the supersonic inlet of an airbreathing launcher", NLR-TR-94-375, 1994.

	Surface triang.		3D Grid Generation			Flow calc.
Grid	nodes	triangles	nodes	elements	edges	time steps
Initial	22275	44546	105786	609338	737396	500
Adapted	30744	61484	222359	1348274	1600926	2000

Table 1: Number of nodes and triangles in the surface triangulation, number of nodes and number of elements in three-dimensional grid for the initial grid and the adapted grid for the AS28G wing/body configuration

Algorithm	cpu-time (initial grid)	cpu-time (adapted grid)	Mflops	computer
Surface triangulation	31m 20s	-	4	SGI-Onyx
3D grid generation	5m 54s	14m 16s	4	NEC SX3
Pre-processing	1m 18s	3m 3s	3	NEC SX3
Flow calculation	46m 11s	8h 5m 6s	253	NEC SX3
Grid adaption	2m 58s	-	5	NEC SX3

Table 2: Cpu-times for the respective algorithmic steps for the AS28G wing/body configuration
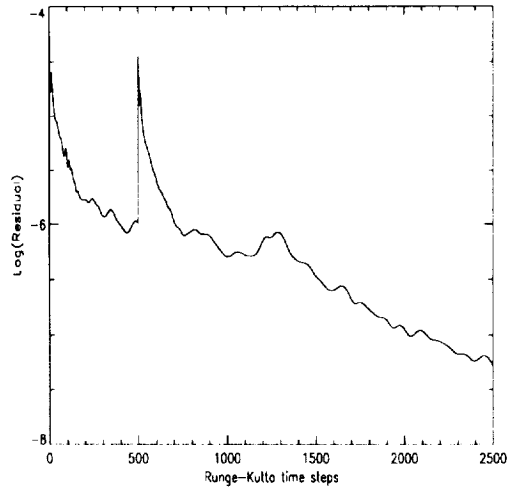
Figure 1: Convergence history of the flow calculation algorithm for the AS28G wing/body configuration on the initial grid and the adapted grid
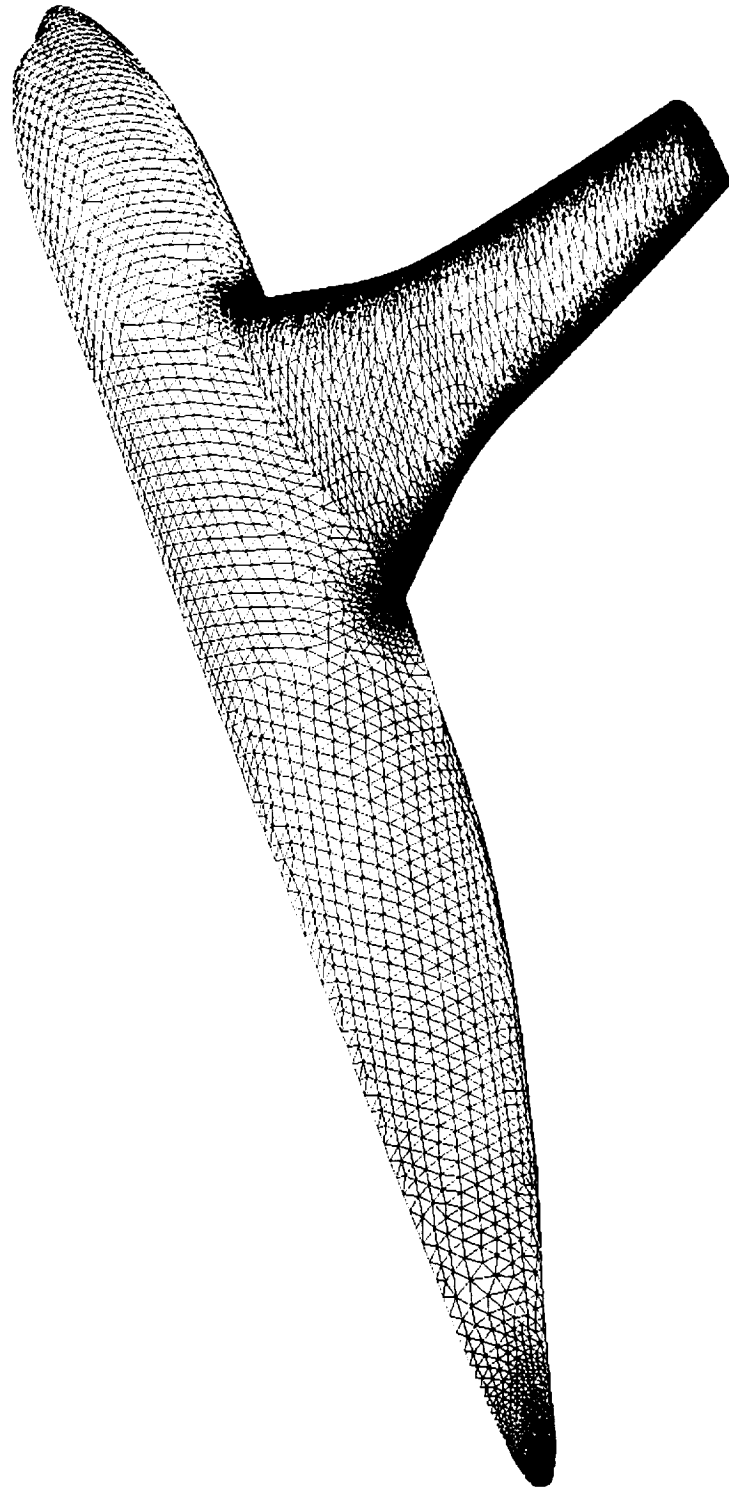
Figure 2: Surface triangulation for the AS28G wing/body configuration
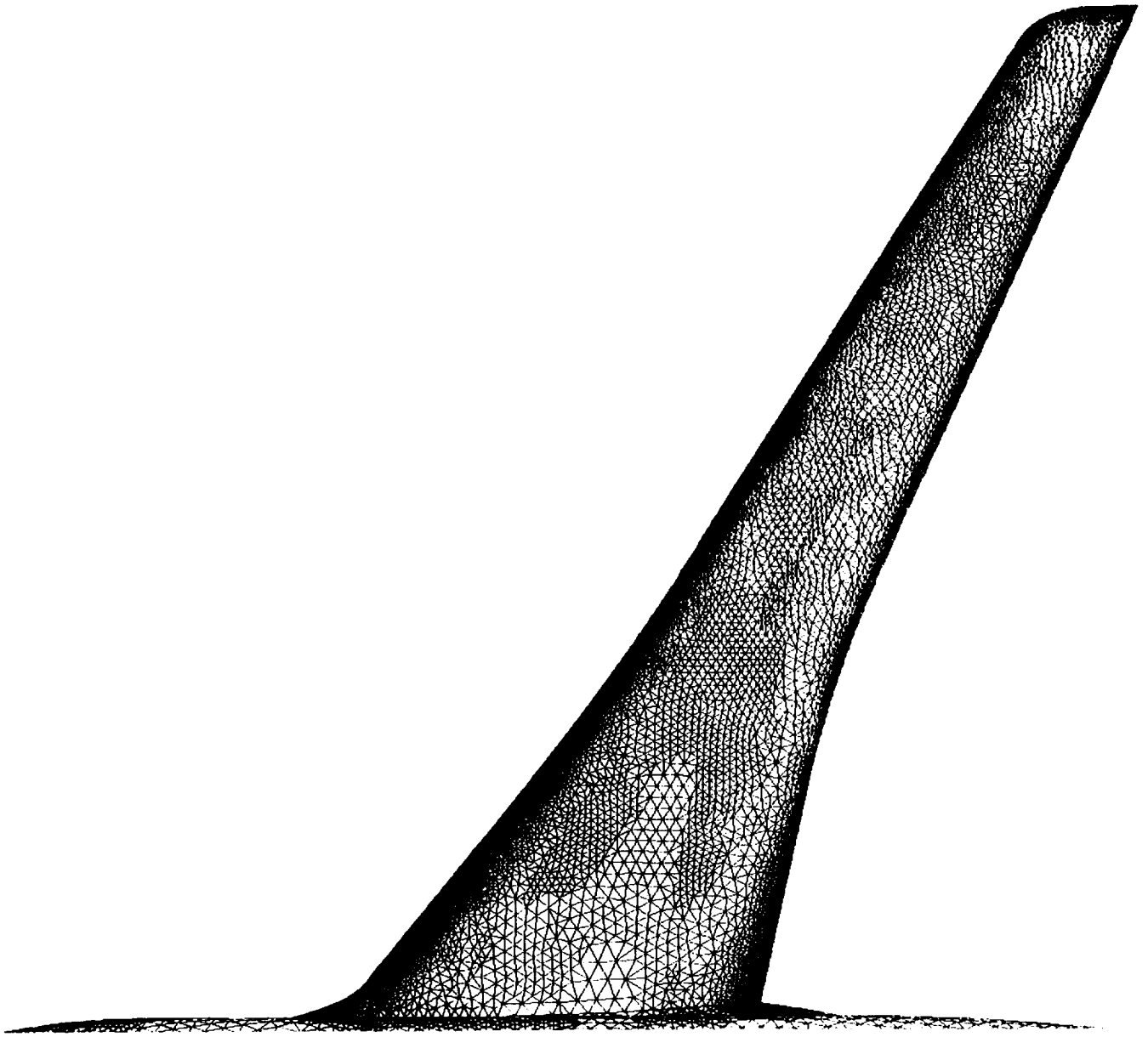
721

Figure 3: Surface triangulation for the AS28G wing/body configuration after one successive refinement
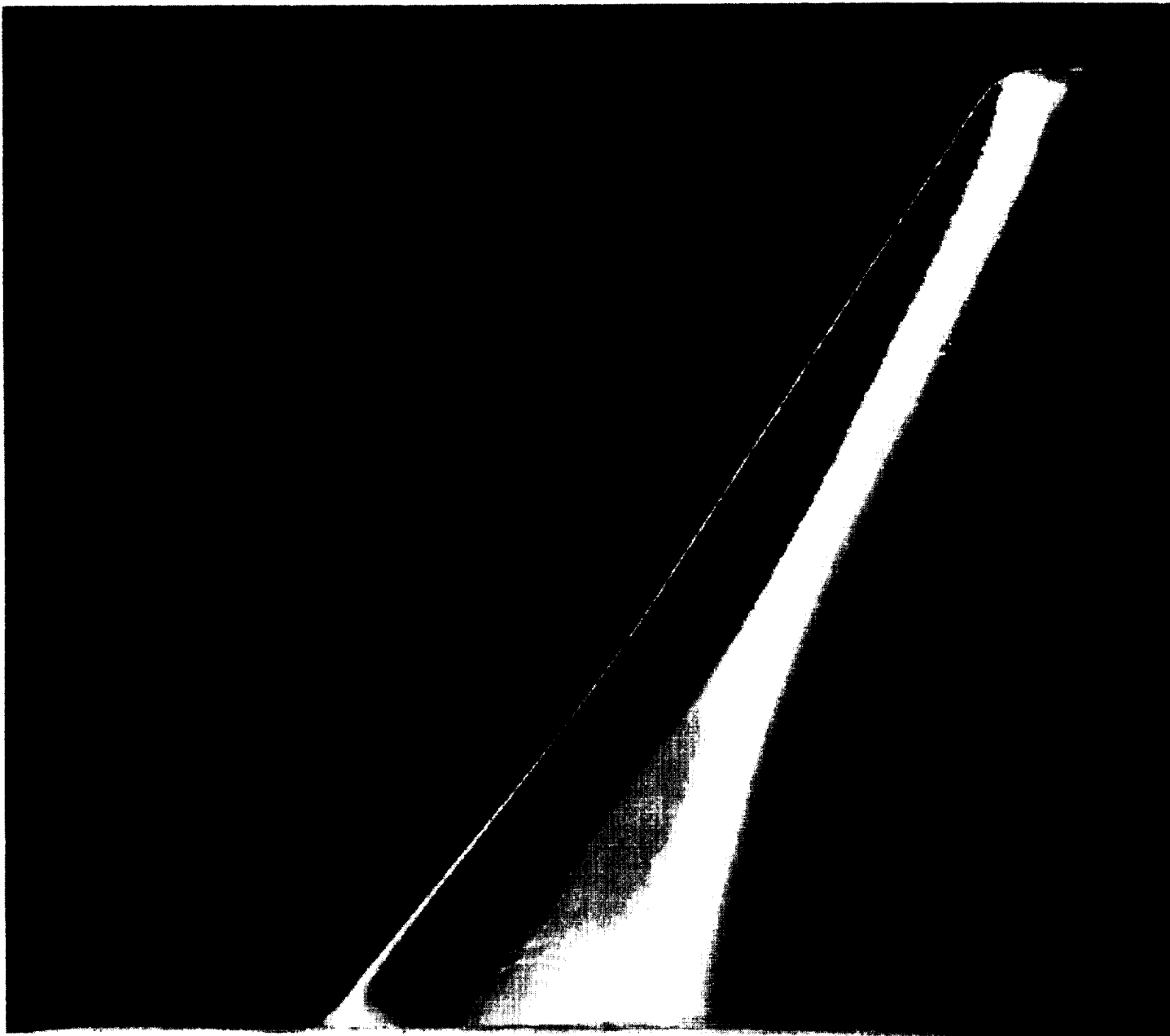
Figure 4: Mach number distribution for the AS28G wing/body configuration on the upper side of the wing after one successive refinement
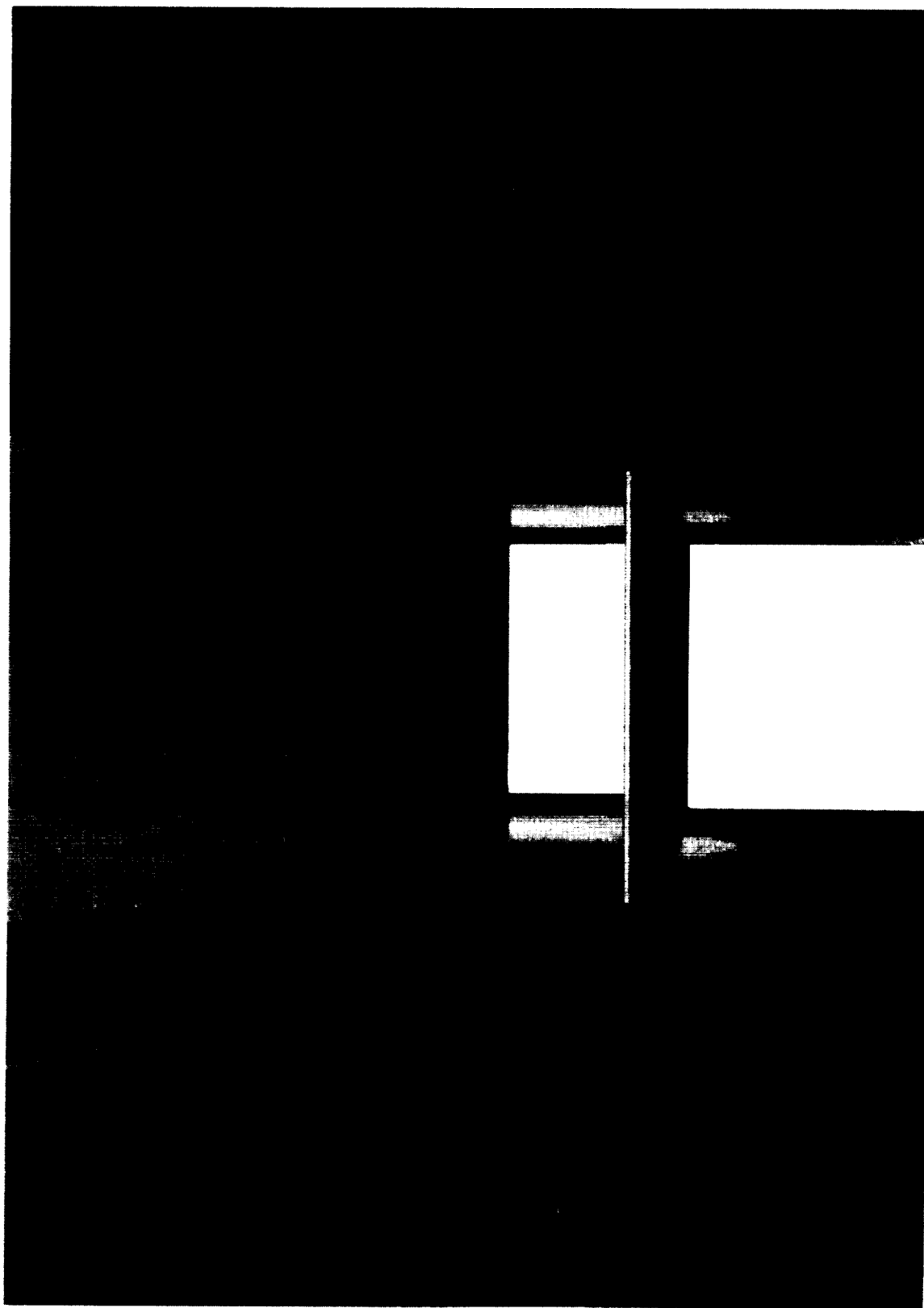
Figure 5: Total pressure distribution scaled with respect to the freestream values for the AS28G wing/body configuration on the upper side of the wing after one successive refinement
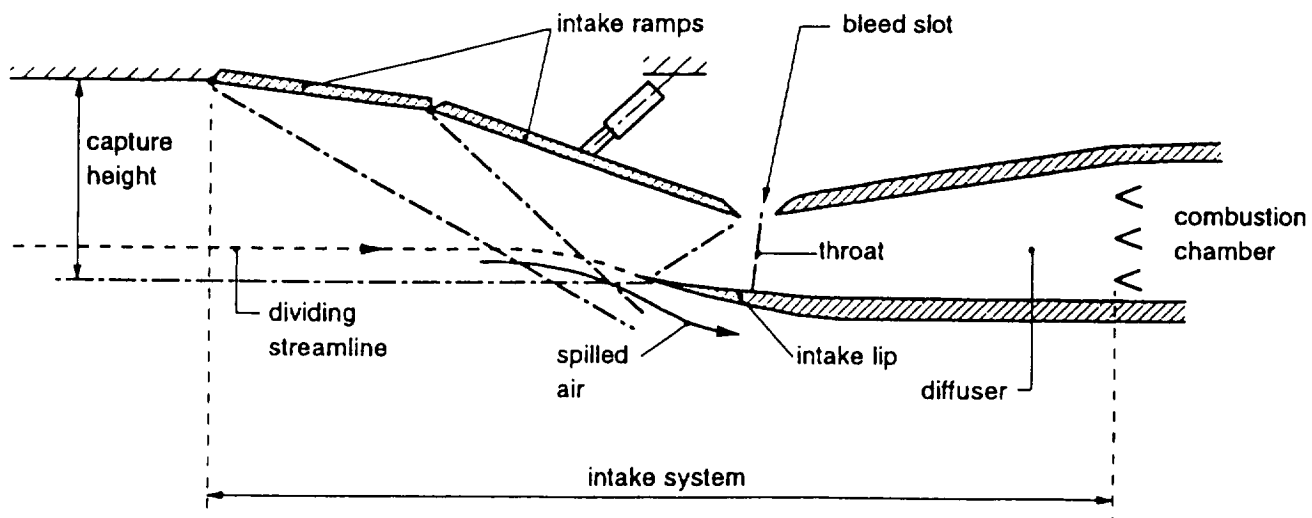
Figure 6: Main inlet components and terminology

Figure 7: Impression of the three-dimensional mixed compression airbreathing inlet geometry modelled by cubic surface and curve representations
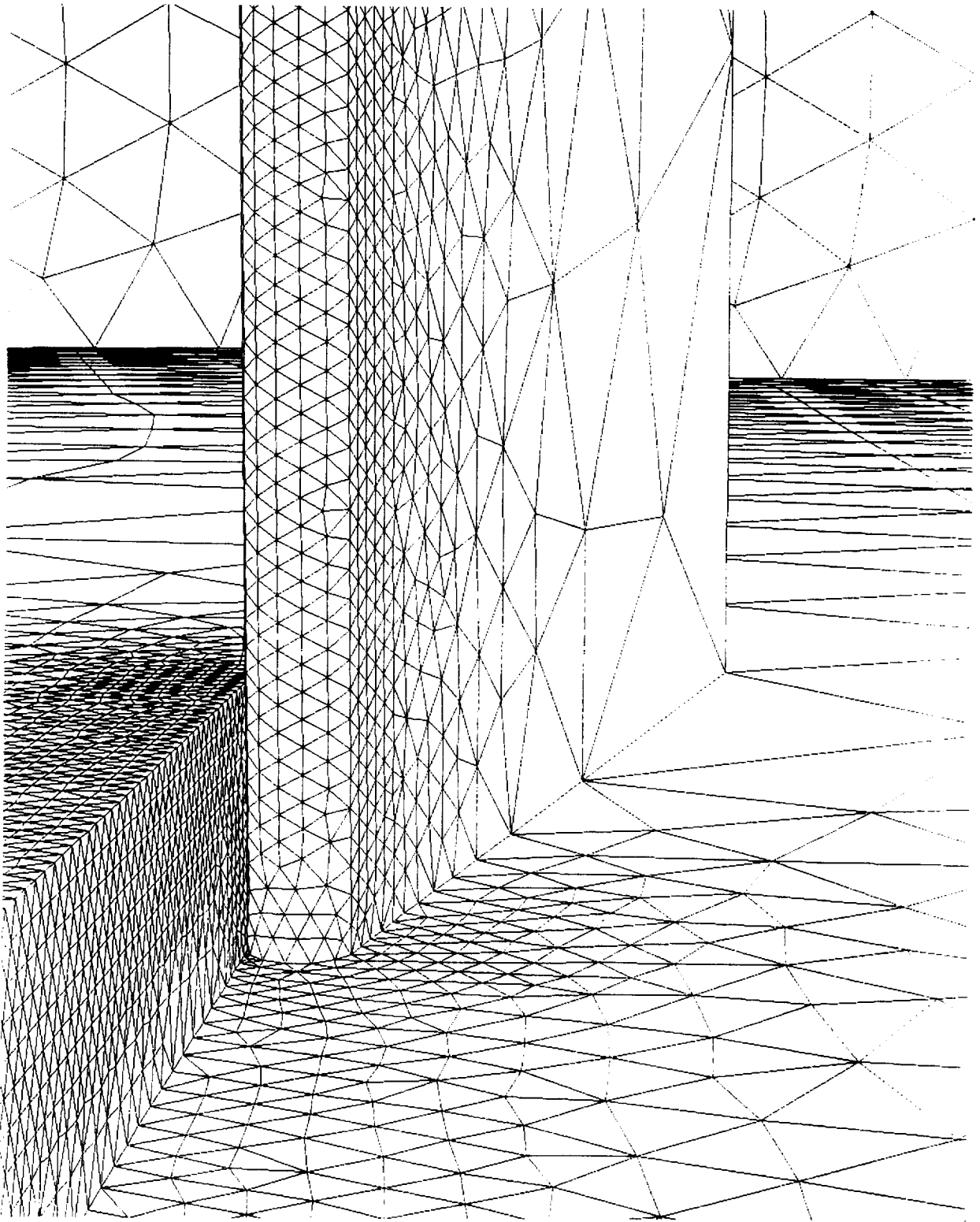
Figure 8: Surface grid at side-wall with refinements at the side wall and the cowl lip

Figure 9: Side view of the Mach number distribution. The flow condition represents "unstarted" flow: strong bow shock and subsonic flow in duct
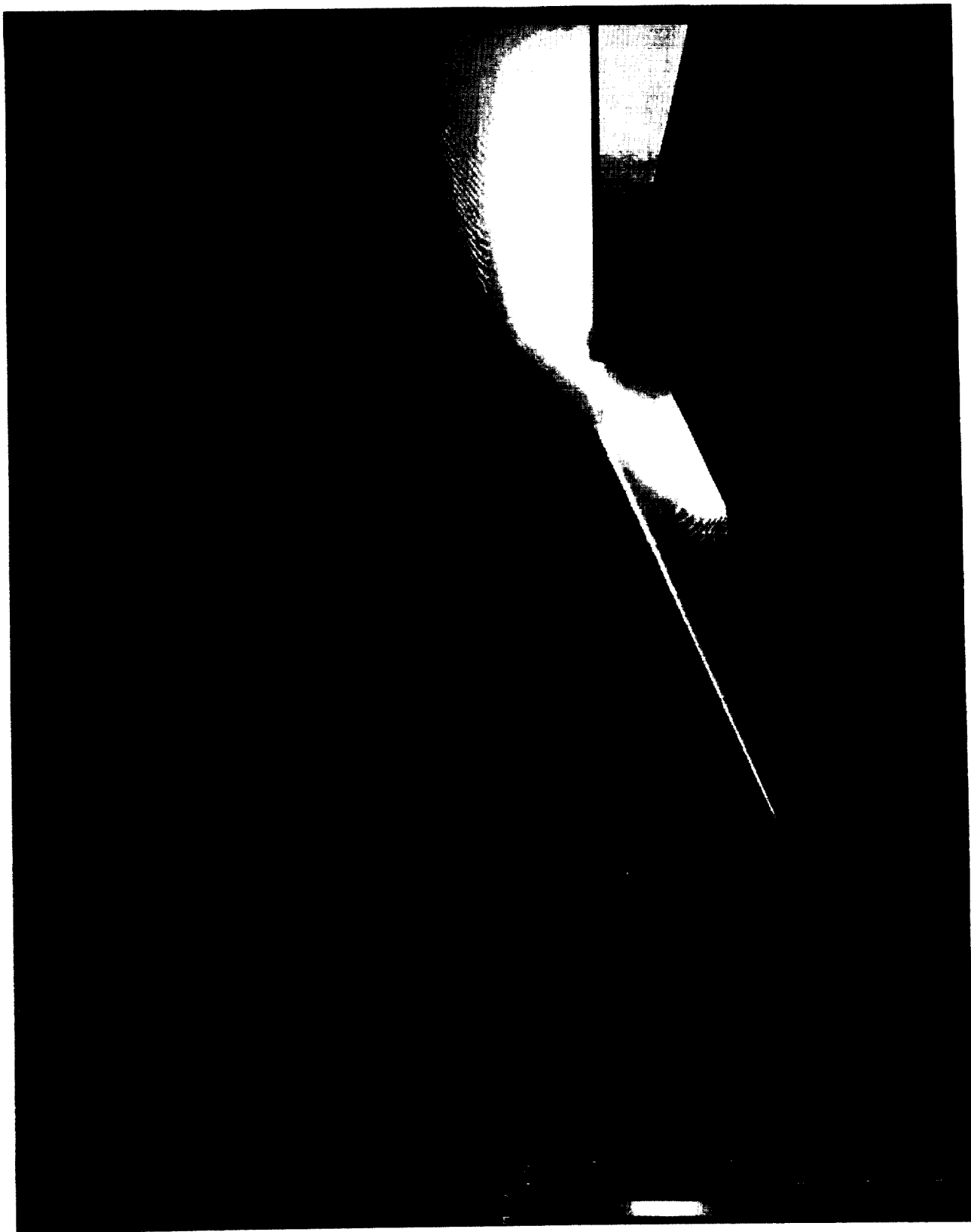
Figure 10: Side view of the Mach number distribution. The flow condition represents "started" flow with a final normal shock in the duct
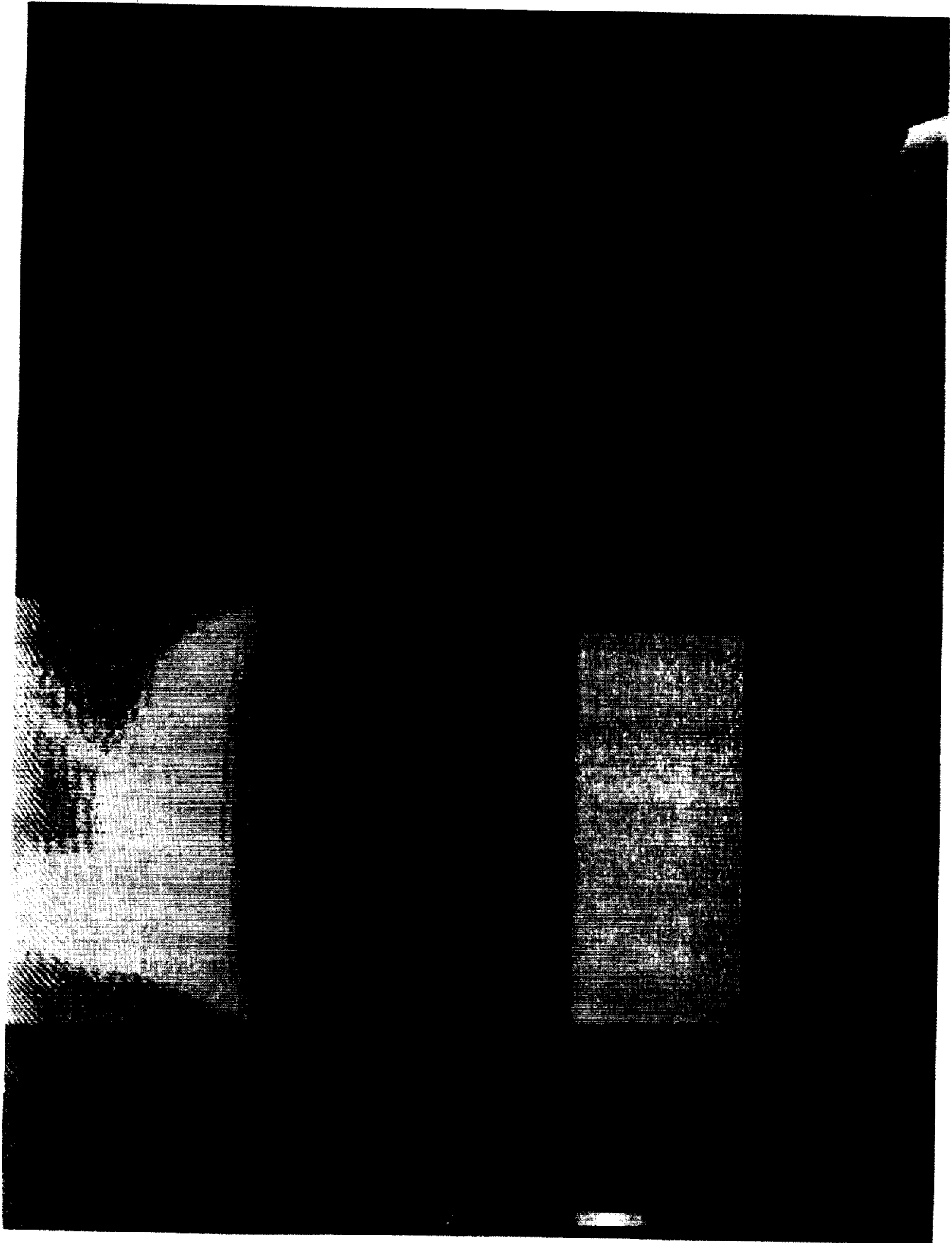
Figure 11: Detailed view of the Mach-number distribution at the intersection of the side-wall ramp and the cowl lip. The flow condition represents "started flow" with a final shock in the duct